Magnetic Separation of Immobilized Biocatalyst Enables Continuous Manufacturing with a Solids-Forming Reaction

Colton E. Lagerman[a]1, Grant D. Marshall[a]1, Matthew A. McDonald[a], Patrick R. Harris[a], Martha A. Grover[a], Ronald W. Rousseau[a], Andreas S. Bommarius*[a]

DOI: 10.1039/x0xx00000x

Supplementary Information

Table of Contents

Additional Results and Discussion

Relative strengths of settling velocities, fluid velocities, and magnetically induced velocities

For particles in low Reynold's number flow, settling velocity can be calculated according to Stokes' law as

$$v_s = \frac{2(\rho_p - \rho_f)gR^2}{9\mu} \#(1)$$

where v_s is the settling velocity of a particle, ρ_p is the density of the particle, ρ_f is the density of the fluid, g is acceleration due to gravity, R is the radius of a spherical particle, and μ is the dynamic viscosity of the fluid. The settling velocities calculated from Stokes' law for different particle sizes are shown in Table S1. For nonmagnetic particles, the time required for settling must be less than the average particle residence time in the device for gravity to affect the separation. Figure S1 shows particle position assuming Stokes' law for settling and particle velocity in the x-direction due to flow for flow rates of 6 mL/min (Figure S1A) and 12 mL/min (Figure S1B). For all particle sizes, settling pulls nonmagnetic particles below the magnetic outlet (dashed line) indicating gravitational settling impacts nonmagnetic particle separation. Settling is especially relevant for 212 µm particles while 60 µm only travel a few millimeters downward across the length of the device. Settling also depends on particle-particle interactions, but these phenomena are outside the scope of this study.

For magnetic particles, the magnetically induced velocity of a particle upward must be greater than or equal to the particle settling velocity ($v_m \geq v_s$) to ensure that magnetic particles remain in the upper half of the device. Magnetically induced velocity (v_m) can be calculated [1] using equ. (2):

$$v_m = \frac{\Delta\chi \Delta H^2 d}{48\eta} \#(2)$$

where $\Delta\chi$ is the difference in magnetic susceptibilities of the particle and fluid and assumed to be 0.027 for iron oxide particles [1], ΔH is the change in magnetic field strength, d is the spherical particle diameter, and η is the fluid viscosity. Thus, the change in magnetic field strength to overcome settling can be calculated as

$$\Delta H \geq \sqrt{\frac{48\eta v_s}{\Delta\chi d}} \#(3)$$

The ΔH required for different sized particles is shown in Table S1. For a particle entering a magnetic field generated by N52 magnets,

$$\Delta H = H_{N52} - 0 \#(4)$$

where H_{N52} is the magnetic field strength generated by N52 neodymium magnets. The magnetic field generated by N52 magnets with dimensions 60 mm by 10 mm by 5 mm, H_{N52}, is approximately 7000 Gauss at the surface of the magnet. For a particle entering the center of the channel 3.5 mm away from the magnets, the magnetic field strength is at a minimum and can be approximated using demagnetization curves where $H$is a function of the magnetic flux density, B [2], calculated as shown in [3]:

$$B = \frac{B_r}{\pi}\tan^{-1}\left(\frac{LW}{2z\sqrt{4z^2 + L^2 + W^2}}\right) - \tan^{-1}\left(\frac{LW}{2(D+z)^2\sqrt{4(D+z)^2 + L^2 + W^2}}\right) \#(5)$$

where B_r is the remanence field of the magnet, L, W, and D are the length, width, and thickness of the magnet, respectively, and z is the distance from the magnet surface. The minimum value for magnetic field strength, *H* in the magnetic separator setup is shown in Table S2 and is much higher than magnetic field strength required to overcome settling.

Iterative device design

The purpose of Device A, Figure S4, was to create a region of simple, fluid flow where the motion of the beads could be easily studied. The device features two inlets, one for the feed slurry and one for a parallel sweeping stream containing no solids which the magnetic particles would be deflected into.

Particle flow simulations included in the SOLIDWORKS computer automated design software were used to estimate the device's performance and determine the expected operating limits of the device. The particle simulations of Device A predicted a perfect separation of the magnetic particles from the nonmagnetic particles when a horizontal magnetic field gradient is applied from a permanent N52 grade magnet. However, experiments shown in Figure 2 indicate the non-magnetic particles also favored the magnetic outlet, likely due to interparticle effects and fluid flow effects. Figure 2 shows the fraction of beads that exited from the outlet closest to the magnet, this bead fraction is referred to as the bead retention because this is the stream that is designed to be recycled back to the reactor. Greater than 90% of magnetic beads were retained, however when a 50-50 mixture of magnetic and nonmagnetic beads were separated, the magnetic bead retention was reduced and decreased with increasing flowrate.

Second Design Iteration (Devices B1 and B2)

The learnings from Device A were applied to the second design iteration resulting in several changes to the separator design. The sweeping stream was removed in favor of a single inlet which is more practical for the intended application. The distance between the two outlets was increased to mitigate the effects of the bead dispersions and clumping observed in the system. To accommodate the larger distance of separation the device was gradually widened from the single inlet to prevent dead zones with zero fluid velocity where particles may accumulate. Devices B1 and B2 were created with slightly different shapes to determine if this significantly affected performance. Finally, the device was designed to utilize gravitational force in the opposite direction of the magnetic force to separate the two particle types instead of just magnetic force to reduce the amount of non-magnetic material exiting in the magnetic stream.

CFD simulations of devices B1 and B2 (Figs. S10, S12) predicted the best separation at feed flows ranging from 8 mL/min to 16 mL/min. The simulation also indicated that the results would not be greatly affected by the slight mixing effects produced by the peristaltic pumps. Since many simulated particles slowed to a low velocity, we suspected bead accumulation within the device would be a significant challenge. In testing, this was confirmed to be problematic. Initially, the magnets were placed above the device to maximize the upward magnetic gradient. However, a large clump of beads formed near the magnets that it forced all solids into the lower outlet. It was discovered that the issue could be mitigated by adjusting the placement of the magnets and the orientation of the device. The magnet placement that worked the best in practice was when they were placed on both sides of the upper part of the device (Figure 2C). This magnet orientation creates a channel where there is only a small force on the magnetic beads, and when the beads begin to settle, the magnetic force will keep them in the channel. Magnetic bead retention was further improved by angling the device so that gravity helped the beads to settle toward the outlets of the device.

The results of devices B1 and B2 were very similar which indicates that the slightly differing shapes did not affect the separation significantly. Separator B1 was selected for further testing because approximately 10% less non-magnetic material exited with the magnetic beads in this device compared to Device B2 (Figs. S11, S13). Separator B1 was tested again with a mixture of crystals and magnetic beads as would be the case in the application system. Figure S15 demonstrates that the magnetic bead recovery decreased when the crystals were added. This is likely due to the different viscosity and density of the amoxicillin solution compared to water or possible due to different interparticle interactions with the needle shaped crystals of various sizes.

The device was also tested with smaller beads of 60 μm average diameter. The second iteration devices were unable to achieve a magnetic bead retention greater than 60% with the smaller beads (data not shown). A third design iteration was necessary to address some of the challenges encountered in the second iteration and improve performance with smaller beads and was used as the demonstrated device in the main text.

Tuning device performance

To further enhance separation performance, device angle (Figure S16) and magnet spacing from the device (Figure S17) were adjusted. By angling the device, the gravitational pull on magnetic particles is reducing, at a maximum angle of 55° below the horizontal, the overall retention of magnetic particles in the magnetic outlet stream is increased at the cost of higher recycled nonmagnetic material. Magnet spacing had little effect on magnetic particle retention (Figure S17). Keeping the magnet as close as possible to the device provides the maximum magnetic field strength to retain beads; however, placing the magnets any closer than 10 mm to the device causes more significant clumping in the separation chamber. As the magnet is moved farther from the device, the magnetic field strength is weaker and likely cause more particle interactions which in turn keeps particles more mixed throughout the device and increases nonmagnetic particle retention in the magnetic outlet. From these studies, the final device configuration utilized highly angled devices with magnets placed against the device with minimal spacing.

pH shift crystallization of amoxicillin trihydrate isolated with magnetic separation

To further verify continuous separation performance, the separation system was next tested on a pilot-scale pH-shift crystallization of amoxicillin trihydrate to demonstrate the removal and recycling of 212 μm beads from a crystallizing slurry. The schematic (Figure S18A) and photograph (Figure S18B) of the setup are shown. The pH-shift crystallization was performed in the presence of 4 g of 212 μm magnetic beads by feeding 45 mM soluble amoxicillin at pH 8.3 and 7 °C into a vessel held at pH 5.8 and 25 °C where amoxicillin solubility is 10 mM to generate supersaturation for crystallization. The slurry, consisting of approximately 50 g/L amoxicillin trihydrate crystals and 13 g/L magnetic particles was fed through the separation system before collecting the final pure crystals in MSMPR-2 held at 4 °C to drive crystallization to completion.

The top outlets of each separator were fed back to MSMPR-1 to demonstrate magnetic bead recovery. The outlets of each device were periodically sampled, and it was found that no magnetic beads passed into the final amoxicillin product in MSMPR-2, demonstrating the separation system operated at 100% separation efficiency for the duration of product collection (Figure S18C). Separator 1 operated consistently between 85 – 95% separation efficiency. With addition of the magnetic trap (Figure S18A), 100% of magnetic particles were recovered or captured in the trap, and no magnetic particles were detected in the isolated amoxicillin trihydrate product (Figure S18E). In addition, only 0.08 g (2%) of the magnetic beads accumulated in the magnetic trap over the course of the 7-hour run.

Amoxicillin trihydrate crystals form long, needle-like crystals and applying a wet mill is ideal to minimize clogging and achieve a more desirable API for downstream processing. To enable wet milling without destroying the magnetic particles, MSMPR-2 was placed after separation and recycle of the magnetic particles. Crystals in MSMPR-2 are wet milled and a small fraction of slurry in MSMPR-2 is sent back to MSMPR-1 to achieve a lower crystal size distribution (CSD) in the overall process at steady state. Crystal growth appears to outpace wet milling for the first 4 hours of operation; however, 100 – 1000 μm chord counts decrease after 4 hours, indicating wet milled crystals in MSMPR-2 eventually lower the chord length distribution of crystals after some lag time (Figure S18D).

The separation system behaved independently of the changing crystal morphology (Figure S18D) in terms of magnetic bead removal (Figure S18E) and the system reached steady state at approximately the 6-hour mark and was operated for two hours past this point. Slurry turbidity decreased over time (Figure S18C) indicating crystal growth from seeds as well as a net removal of crystal mass from the system relative to the rate of crystal mass generation by pH shift. The decrease in chord length over the course of the run (Figure S18D) could indicate selective removal of larger crystals from the system or a lag time in the effects on crystal size by wet milling.

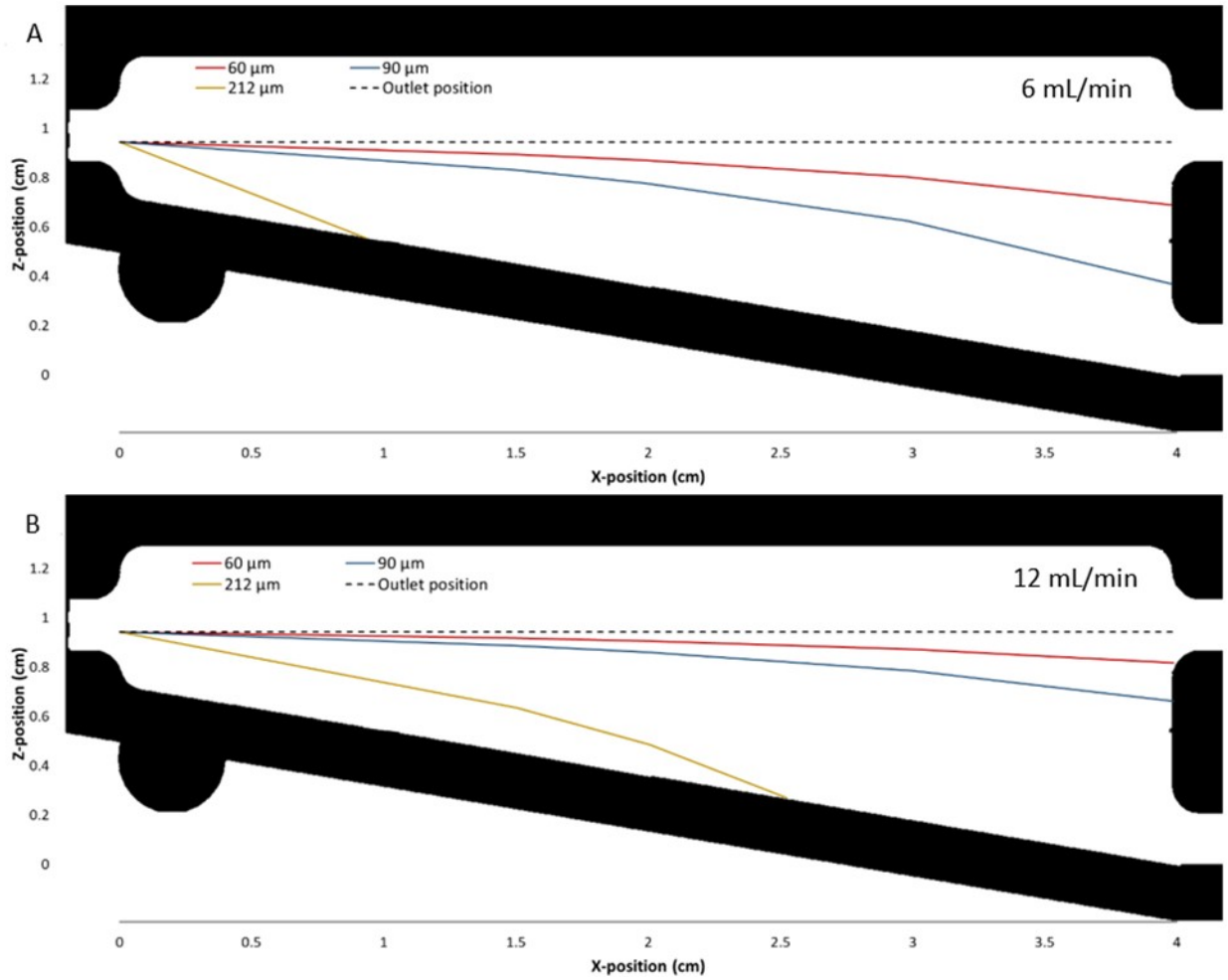

Figure S1. The trajectories of single beads with diameters of 60 µm (red), 90 µm (blue) and 212 µm (yellow) as they flow through the device. X-positions are calculated from fluid velocity generated by flow rates of either A) 6 mL/min or B) 12 mL/min. Z-positions of the particles are calculated using settling velocities from Stokes' law and the time required to travel along the length of the device.

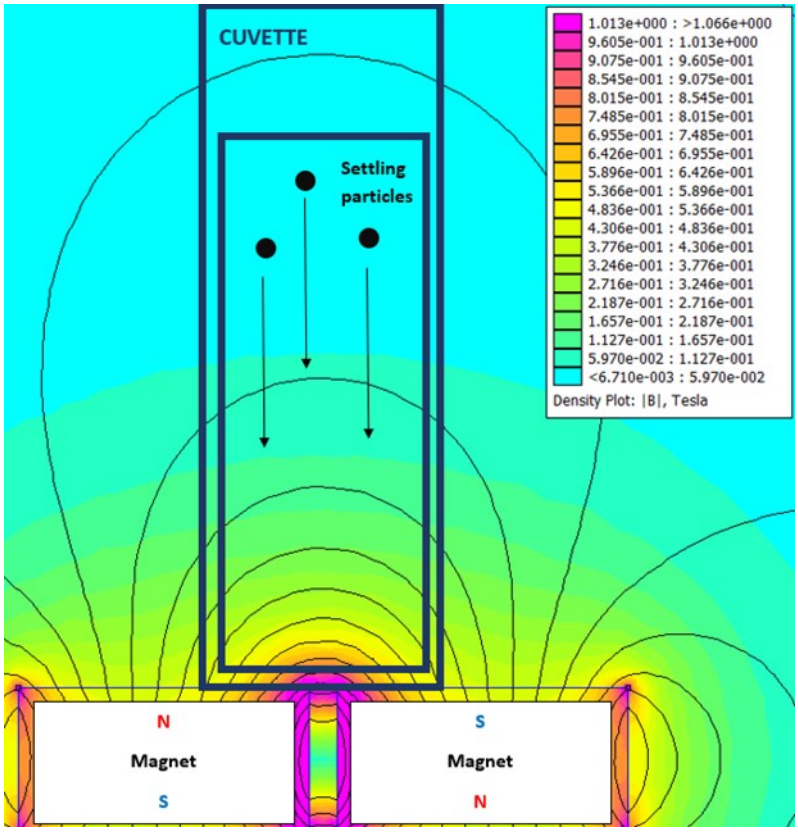

Figure S2. Magnetic field simulations from Octave Finite Element Method Magnetics (FEMM) replicating the magnetic field used in magnetic bead settling experiments in different solutions in a cuvette. The magnets used for the 212 µm diameter beads settling experiments and simulated here are 10 mm by 5 mm with a 2 mm gap between the magnets.

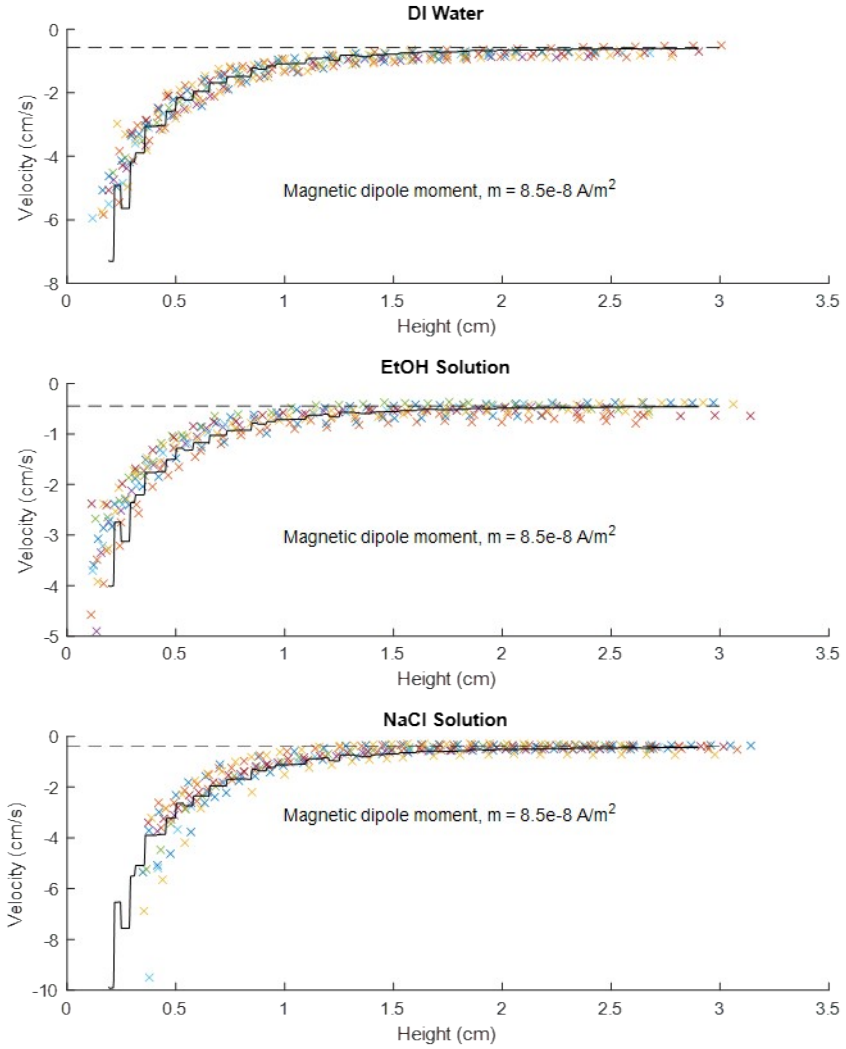

Figure S3. Settling velocities for magnetic particles in DI water, ethanol, and sodium chloride solutions. Velocity is tracked as a function of distance from the magnet. Each particle tracked is shown in a different color in each plot. The fit for magnetic dipole moment is shown as a black line. A constant magnetic dipole moment of 8.5e-8 A/m2 was shown to describe the system well and this value was validated because the fit was maintained with the experiments in EtOH and NaCl solutions. The jagged fit line is due to the finite element method simulation of the magnetic field given by Octave FEMM. This experiment shows that the magnetic force on these particles may not have a significant effect beyond 1 cm distance from the magnetic surface, limiting the design of the separator using small, neodymium magnets.

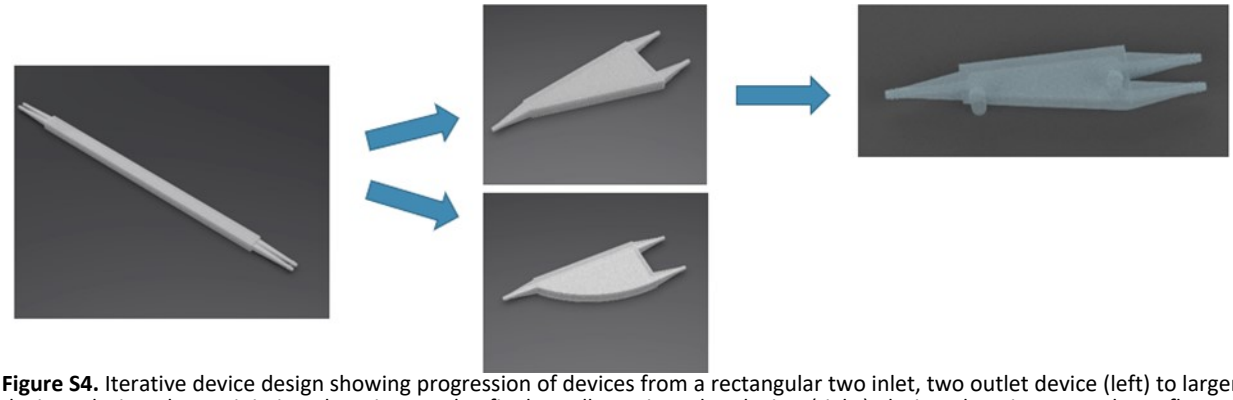

Figure S4. Iterative device design showing progression of devices from a rectangular two inlet, two outlet device (left) to larger triangular devices designed to minimize clumping to the final smaller, triangular device (right) designed to increase slurry flow rate. In the supplemental text, devices are referred to as Device A (left), Devices B1 and B2 (middle), and Device C.

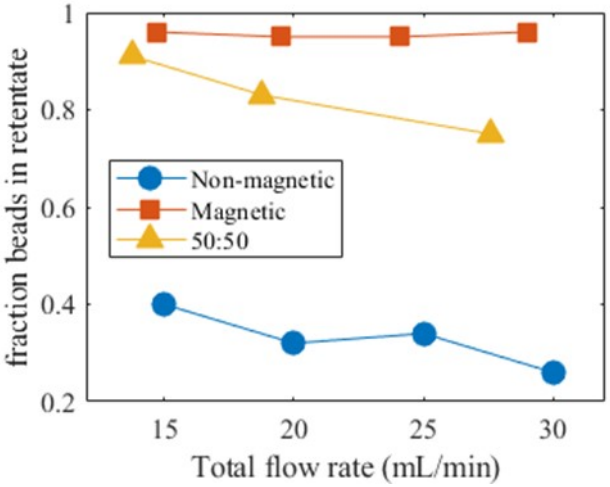

Figure S5. Performance of Device A using 212 µm average diameter beads measured by fraction of beads leaving the retentate stream. In addition to the 50:50 mixture of non-magnetic and magnetic beads (yellow), two control studies were conducted: magnetic beads only

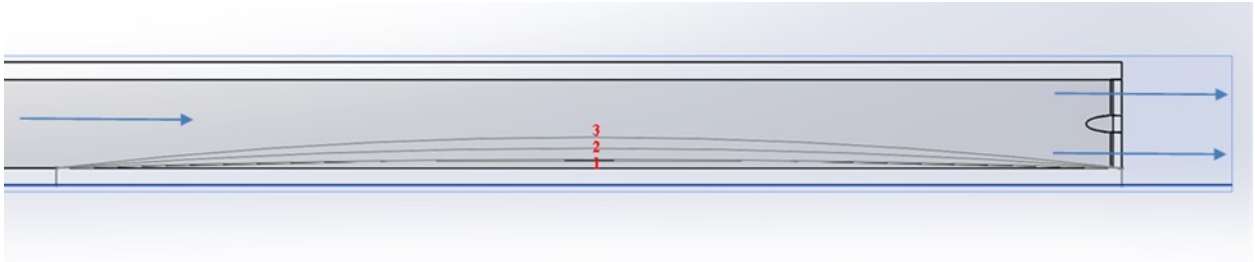

(red) and non-magnetic beads only (blue). The addition of non-magnetic beads reduces the overall separability of magnetic beads.

Figure S6. Simulated fluid flow entering Device A at 160 mm3/s (9.6 mL/min) total with 3 different height bead clumps. These clumps simulate accumulation of magnetic beads on the surface where the magnet is placed (bottom). Clumps were made with an arc that spanned 6 cm (length of magnet), with highest point in the middle (3 cm from the outlet). Max height tabulated in Table S5.

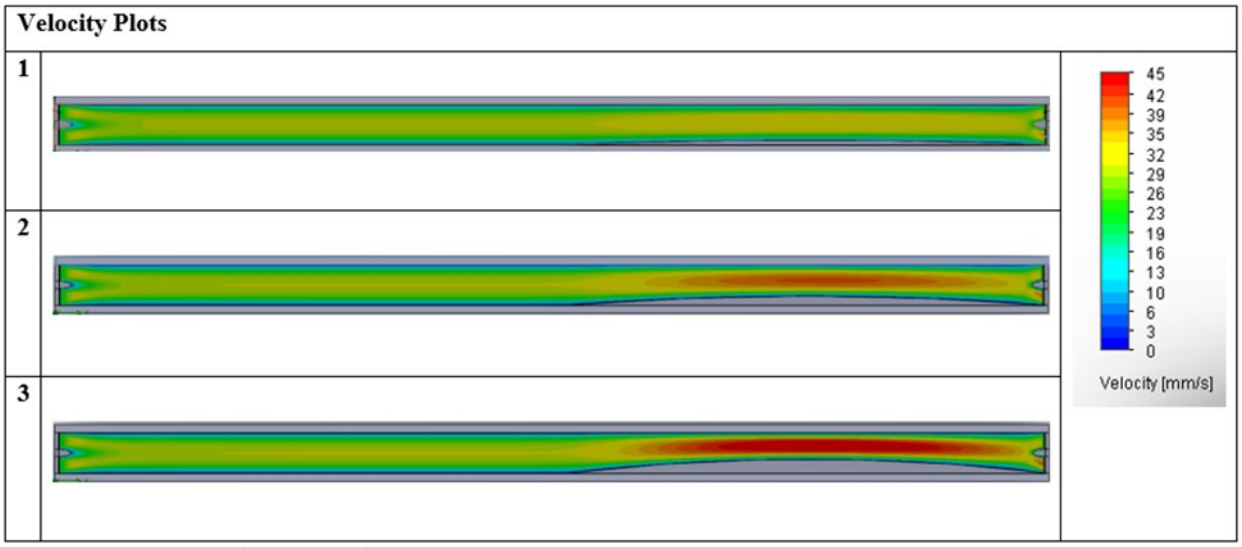

Figure S7. Velocity gradient calculated for each simulated bead clump from accumulating magnetic beads near the magnet placed on the bottom wall of the device. Velocity is significantly increased around the bead clump, which in turn causes additional mixing and reduced separation efficiency. A particle with magnetic interaction was not simulated.

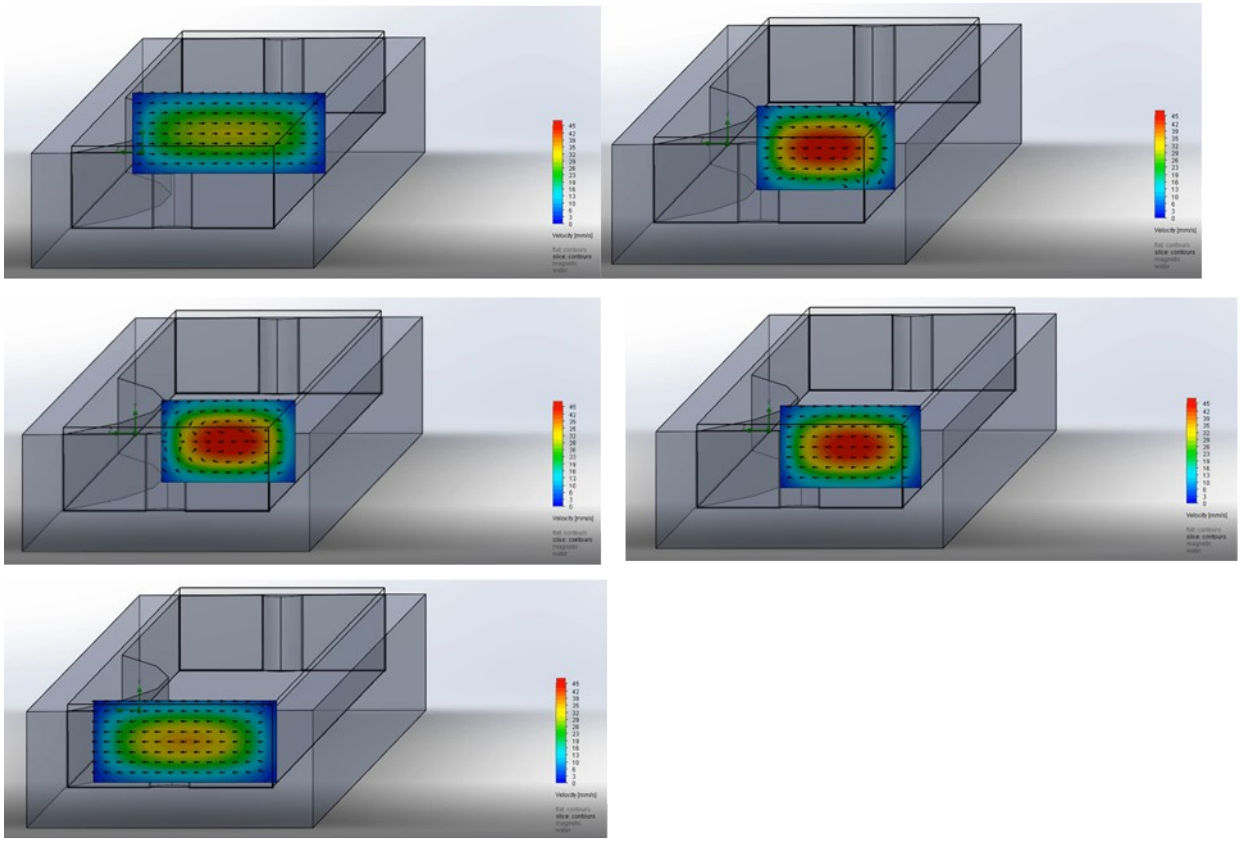

Figure S8. Cross sectional velocity plots at different positions over the length of the bead clump show change in velocity vector direction, likely increasing mixing and reduction in separation efficiency. (A) Velocity vectors are symmetrical at first, then (B) point to the non-magnetic outlet on the first half of the bead clump due to the decreasing width of the device causing increased directional flow velocity. (C) Velocity vectors at the max height of the bead clump are highly asymmetrical, likely causing the most mixing before (D), (E) switching direction to point to the magnetic outlet on the second half of the bead clump due to the expanding chamber.

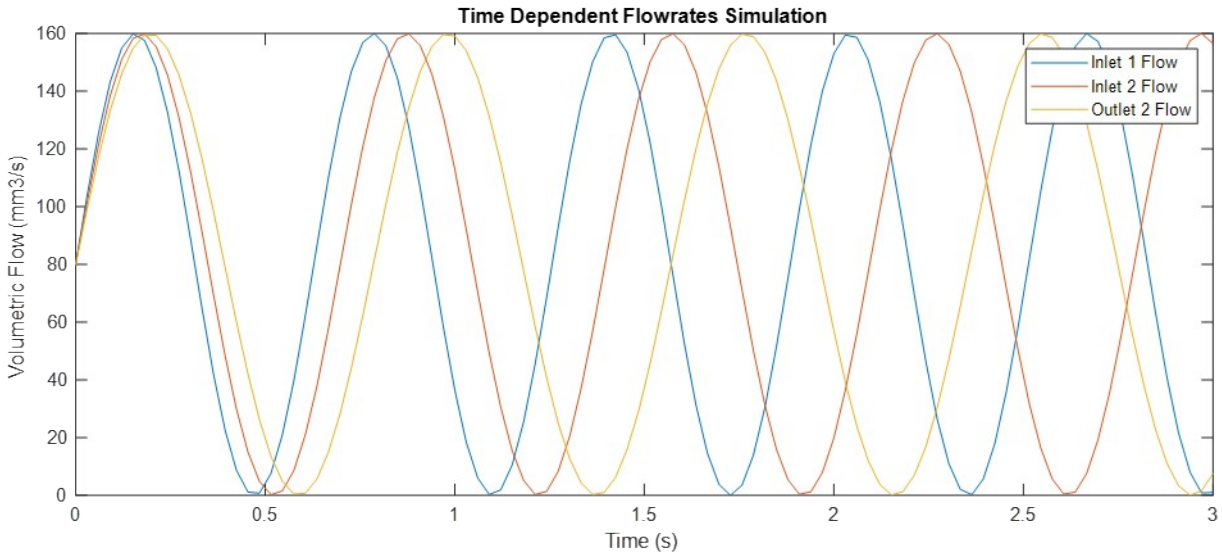

Figure S9. Graph of sinusoidal flow pattern generated by peristaltic pumps used in experiments. By design, the peristaltic pumps used in the experiments pump fluid in a sinusoidal pattern. As the sinewaves of the 3 pumps (2 at inlet, 1 at magnetic outlet) go in and out of phase, many different flow patterns are generated. A time-dependent simulation was calculated with the following boundary conditions: (i) Total time: 3 seconds (ii) Inlet 1 volume flow = 80sin(10t) + 80 [mm3/s] (iii) Inlet 2 volume flow = 80sin(9t) + 80 [mm3/s] (iv) Magnetic outlet volume flow = 80sin(8t) + 80 [mm3/s] (v) Non-magnetic outlet boundary condition: Atmospheric Pressure (vi) Convergence goal at each timestep: Inlet Mass Flux – Outlet Mass Flux = 0

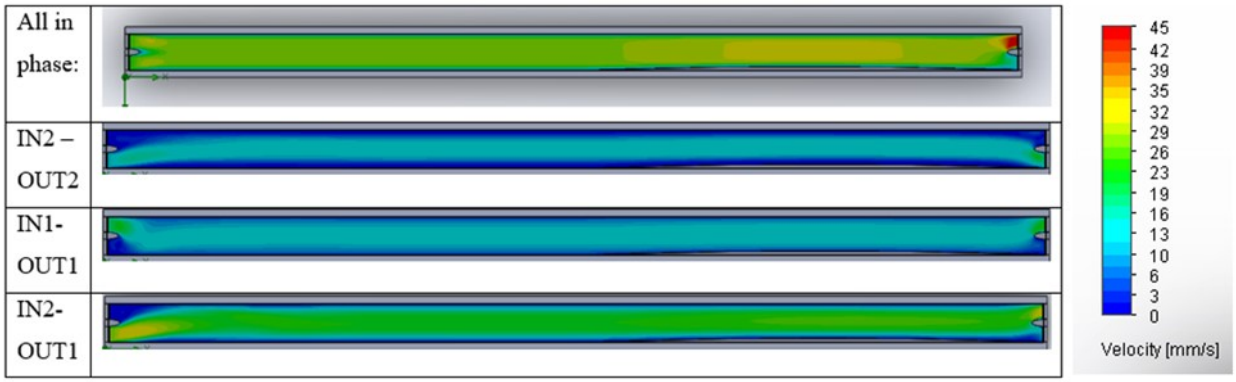

Figure S10. Velocity plots showing results of pumps falling out of sync using equations generated in Figure S8. At t < 0.5 s, pumps are in phase. Over the next few seconds, the pumps fall out of sync and higher velocities oscillate from the bottom inlet (IN2) – magnetic outlet (OUT2) to the top inlet (IN1) – top outlet (OUT1) to finally IN2 – OUT1. This cycle repeats as the flow patterns for the pumps fall in and out of sync which adds to the mixing nonidealities observed experimentally.

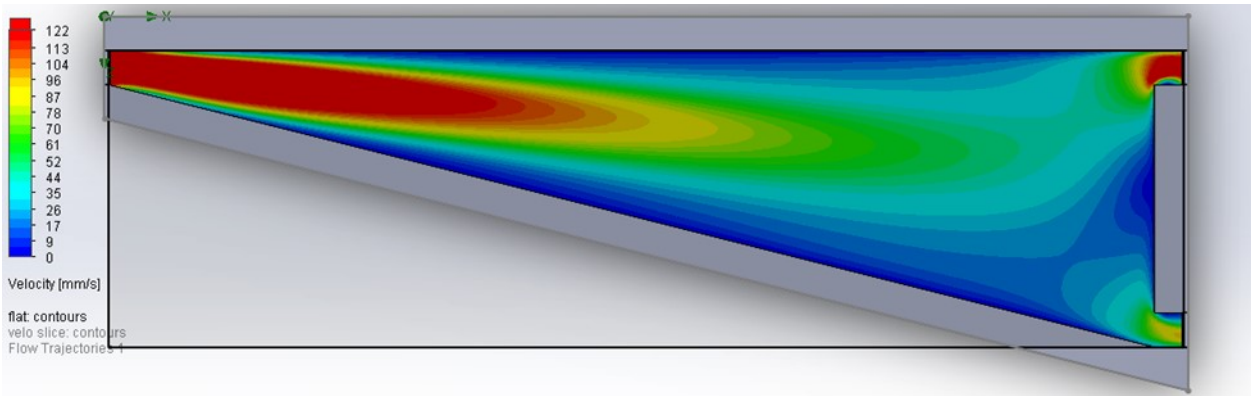

Figure S11. CFD simulations of fluid velocity through Device B1.

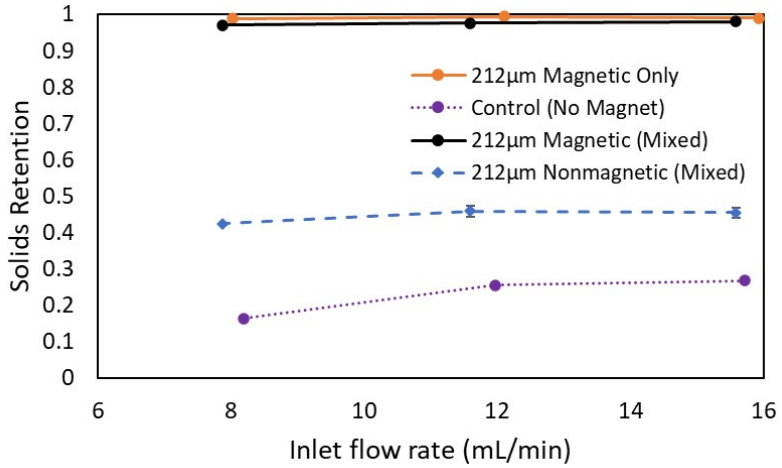

Figure S12. Solids retention data is shown for separation of magnetic and nonmagnetic beads of 212 µm average diameter in Device B1. Flow rate has little effect on separation performance; however, with increasing flow rate, the fraction of nonmagnetic beads retained (i.e., exiting the magnetic outlet) increases. The control experiment (dotted purple line) was performed with only magnetic particles without a magnet placed on the device.

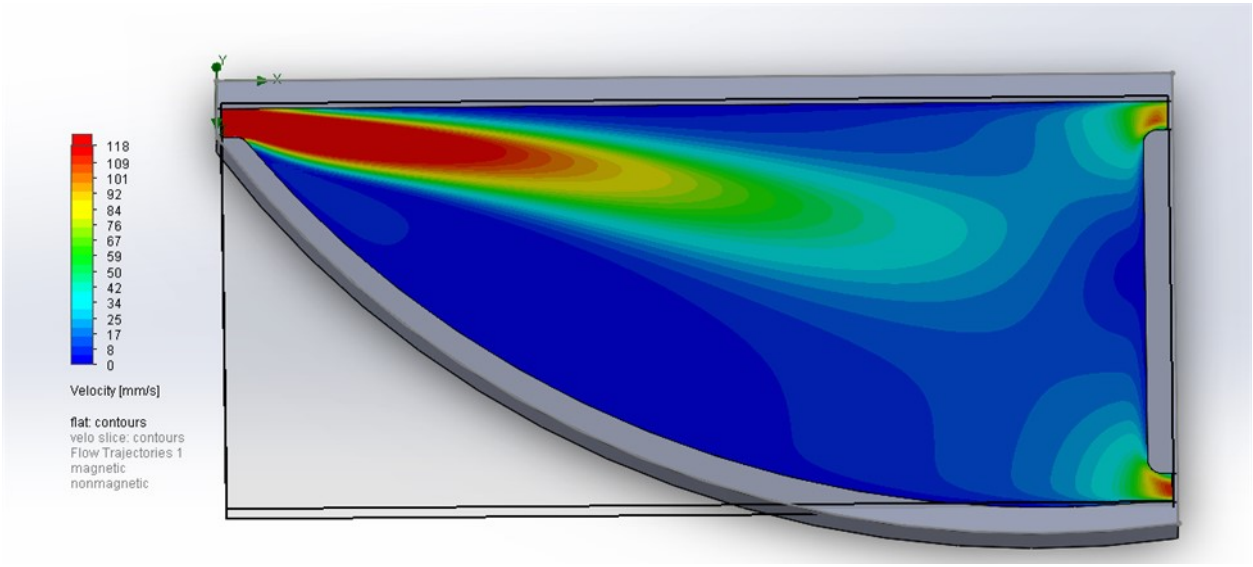

Figure S13. CFD simulations of fluid velocity through Device B2. When compared to Device B1, the additional volume from the rounded bottom surface increases dead zone volume in the device.

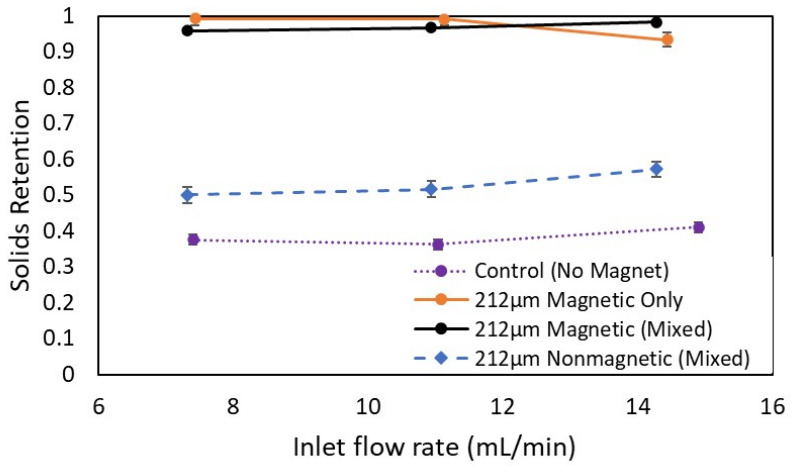

Figure S14. Solids retention data is shown for separation of magnetic and nonmagnetic beads of 212 µm average diameter in Device B2. Flow rate has little effect on separation performance except at the highest flow rates; however, with increasing flow rate, the fraction of nonmagnetic beads retained (i.e., exiting the magnetic outlet) increases and is higher than nonmagnetic beads retained in Device B1. The control experiment (dotted purple line) was performed with only magnetic particles without a magnet placed on the device.

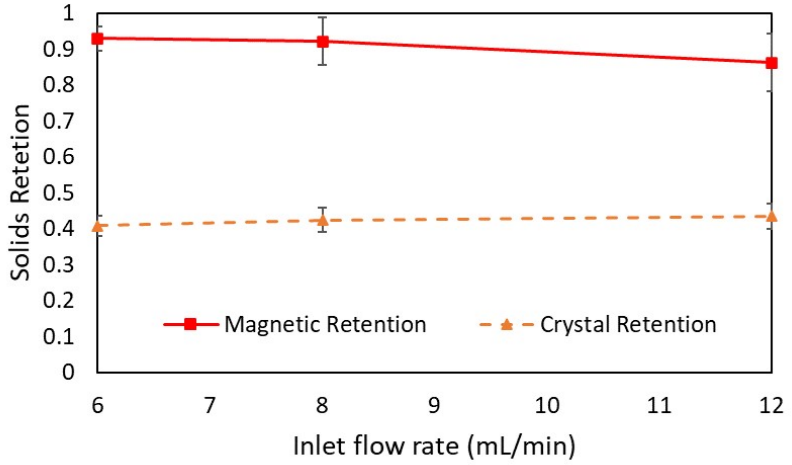

Figure S15. Solids retention data for separation of 212 µm average diameter beads from amoxicillin crystals in Device B1. Magnetic bead retention is lower when compared to separation of magnetic and nonmagnetic beads and is lowest at 12 mL/min.

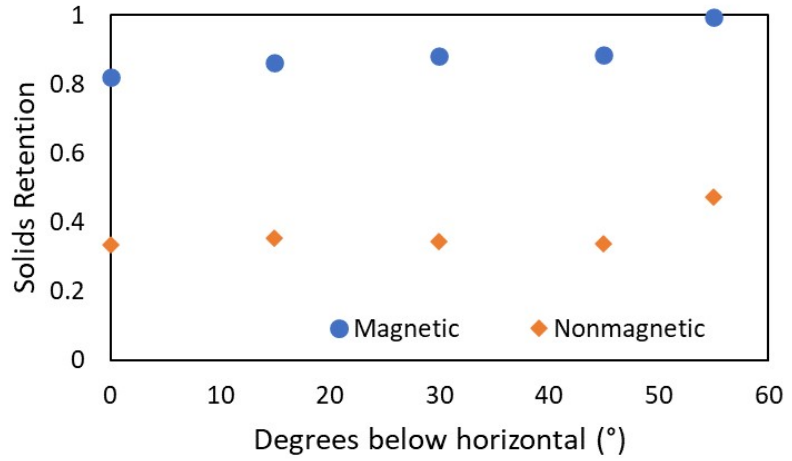

Figure S16. Solids retention data for separation of 212 µm average diameter magnetic and nonmagnetic particles as a function of device angle measured as degrees below the horizontal.

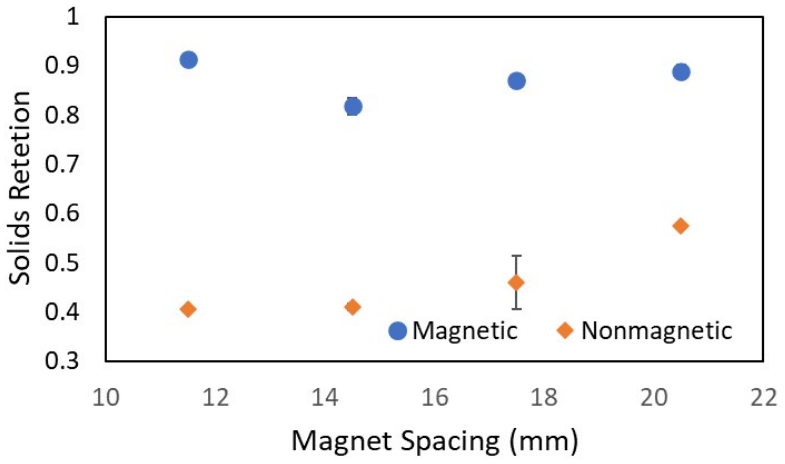

Figure S17. Solids retention data for separation of 212 µm average diameter magnetic and nonmagnetic particles as a function of magnet spacing.

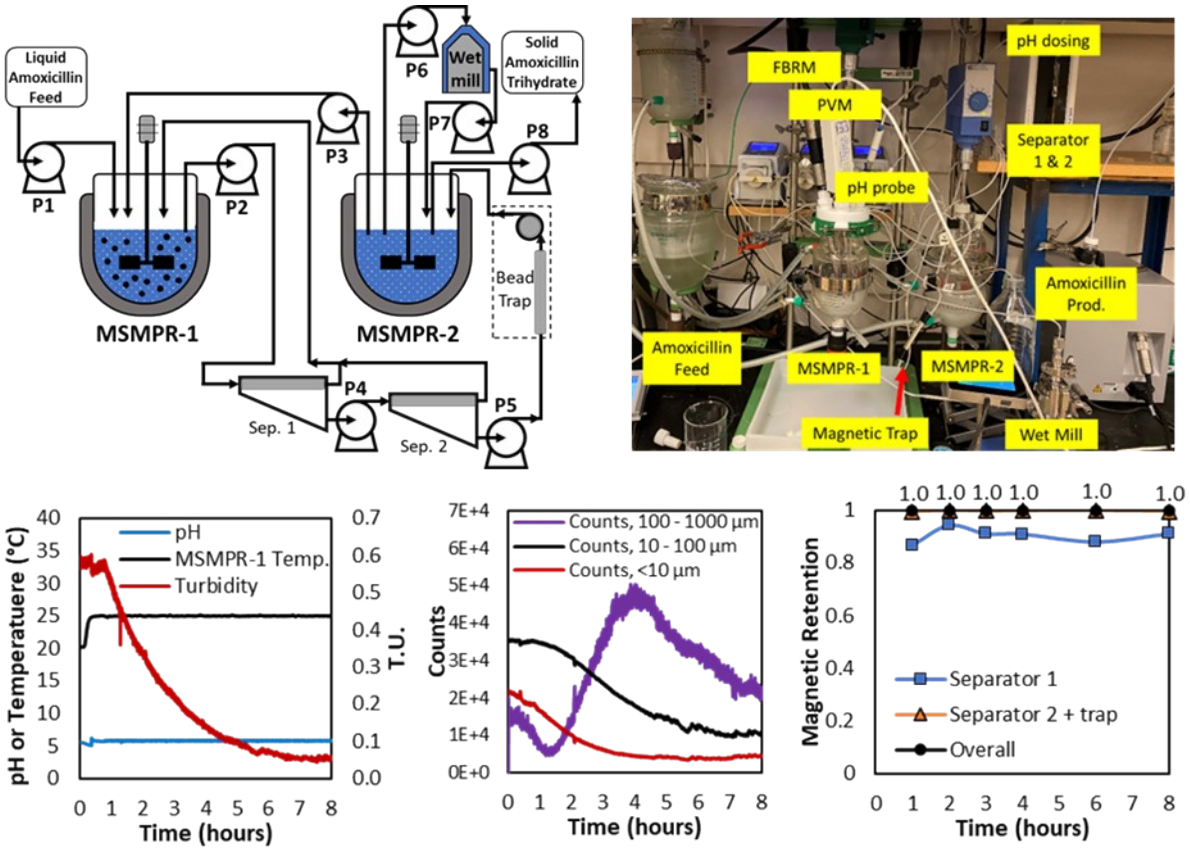

Figure S18. (A) Process flow diagram for pilot-scale pH shift crystallization of amoxicillin trihydrate (B) Picture of pilot plant setup with labeled unit operations (C) pH value, temperature, and turbidity measurements over the course of the 8-hour pilot plant run. (D) Crystal chord length counts for bins of < 10 µm, 10 – 100 µm, and 100 – 1000 µm as measured by FBRM. The 100 – 1000 µm counts are reported as Counts x102. (E) Magnetic bead retention for both separators and magnetic trap are reported over the course of the 8-hour pilot run.

Table S1. Change in magnetic field strength required ($\Delta H_{required}$) to overcome settling velocities (vs) of iron oxide particles of various diameters in water calculated from Equations (1) – (3).

d (µm)	v_s (cm/s)	η (poise)	$\Delta\chi$	$\Delta H_{required}$ (Oe)
60	0.07	0.01	0.027	14
90	0.15	0.01	0.027	17
212	0.83	0.01	0.027	26

Table S2. Magnetic field strength generated by N52 grade neodymium magnets at the center line of the channel in the device, 3.5 mm from the magnets. The remanence field, B_r, is a physical property of the magnet, B is calculated using Equation 5, and H_{N52} is evaluated using demagnetization curves for N52 grade neodymium magnets.

z (mm)	B_r (Gauss)	B (Gauss)	H_{N52} (Oe)
3.5	14000	4200	9000

Table S3. Parameters used in particle settling studies to calculate magnetic dipole moment for 212 µm average diameter particles.

VARIABLE	DESCRIPTION	NOTE
ρ_p	Particle density	1.2 g/cc
g	Gravity	9.81 m/s2
d_p	Particle diameter	212 - 250um
m	Magnetic dipole moment	Unknown property of the particles, difficult to measure directly
B	Magnetic Flux density	Obtained from simulation software
ρ_f	Fluid density	See Table 2
C_D	Drag coefficient	=24/Re for low Re, or get from other correlations
u	velocity	Terminal settling velocity

Table S4. Measured settling velocities under gravity only for 212 µm average diameter particles in various buffers measured by slow motion video analysis. Densities and viscosities are literature values for each solution at 25 °C.

Solution	**Density (g/mL)**	**Viscosity (cP)**	**Measured Settling Velocity w/o Magnetic Force (cm/s)**
DI water	0.99984	1.0002	-0.60 +/- .01
Saline Solution	1.1008	0.709	-.407 +/- .008
Ethanol Solution	0.9086	1.900	-.448 +/- 0.012

Table S5. Maximum heights for simulated bead clumps shown in Figure S5.

Bead clump Max Height
#1 = 0.5 mm (about 2-3 layers of beads)
#2 = 1.15 mm (about 6-8 layers of beads)
#3 = 1.75 mm (about 10-12 layers of beads)

References

[1] C. B. Fuh, M. H. Lai, L. Y. Lin, S. Y. Yeh, *Analytical Chemistry* **2000**, *72*, 3590-3595.
[2] L. Li, G. Yang, Q. Sun, *Journal of Magnetism and Magnetic Materials* **2021**, *537*, 168158.
[3] G. Alberts, H. Hollis, H. Labollita, G. Mueller, *UF Journal of Undergraduate Research* **2019**, *20*.